Partitioning of Co^{2+} and Mn^{2+} into meridianiite ($MgSO_4 \cdot 11H_2O$): Ternary solubility diagrams at 270 K; cation site distribution determined by single-crystal time-of-flight neutron diffraction and density functional theory

A.D. Fortes [a, b, c, *], I.G. Wood [b], K.A. Hudson-Edwards [c], M.J. Gutmann [a]

[a] ISIS Facility, STFC Rutherford Appleton Laboratory, Harwell Science and Innovation Campus, Chilton, Didcot, Oxfordshire, OX11 0QX, UK
[b] Department of Earth Sciences, University College London, Gower Street, London WC1E 6BT, UK
[c] Department of Earth and Planetary Sciences, Birkbeck, University of London, Malet Street, London WC1E 7HX, UK

ARTICLE INFO

ABSTRACT

We have grown single crystals of $M^{2+}SO_4$ hydrates at 270 K from aqueous solutions in the ternary systems $CoSO_4-MgSO_4-H_2O$ and $MnSO_4-MgSO_4-H_2O$. These systems exhibit broad stability fields for a triclinic undecahydrate on the Mg-rich side (i.e., Co- or Mn-bearing meridianiite solid solutions) and stability fields for monoclinic heptahydrates on the Mg-poor side (i.e., Mg-bearing solid solutions of bieberite or mallardite). The solubility curves and distribution coefficients, describing the partitioning of M^{2+} ions between liquid and solid phases, have been determined by thermo-gravimetric and spectroscopic techniques. A subset of $M^{2+}SO_4 \cdot 11H_2O$ specimens were selected for single-crystal time-of-flight neutron diffraction analysis in order to evaluate preferential occupancy of symmetry-inequivalent coordination polyhedra in the structure. Considering the nearly identical dimensions of the first coordination shells, there is a surprising difference in the distribution of Co and Mn over the two available sites.
© 2017 The Author(s). Published by Elsevier B.V. This is an open access article under the CC BY license (http://creativecommons.org/licenses/by/4.0/).

1. Introduction

1.1. Scientific background

Magnesium sulfate forms a large number of crystalline hydrates, $MgSO_4 \cdot nH_2O$ with $n = 1$, 1¼, 2, 2½, 3, 4, 5, 6, 7, 9 and 11, many of which occur naturally as minerals. Of these hydrates, only kieserite ($n = 1$), hexahydrite ($n = 6$), epsomite ($n = 7$), and meridianiite ($n = 11$) are known to be stable in contact with aqueous $MgSO_4$ solution; the other phases generally occur under conditions of reduced water activity, either very low humidity, or in methanolic or acidified solutions [36], or else are formed under extreme disequilibrium conditions, such as rapid quenching of aqueous

solution in liquid nitrogen [19,20,24]. Other divalent metal sulfates, including $ZnSO_4$, $NiSO_4$, $CuSO_4$, $CoSO_4$, $MnSO_4$, and $FeSO_4$ also form a range of crystalline hydrates, many of which are isotypic with the Mg^{2+} analogue. Furthermore, there is extensive substitution possible amongst these compounds, including complete solid solution between many isostructural end-member species [39]. Amongst these divalent metal sulfates, however, only a single 'cryohydrate' — with $n = 11$, meridianiite — is known thus far to exist [55]. This species has a small stability field in aqueous solution at atmospheric pressure, between a eutectic at 269 K and a peritectic at 275 K, where it decomposes into $MgSO_4 \cdot 7H_2O$ + liquid. The stability field of meridianiite may expand to as much as 30 K at pressures of 200 MPa [25].

No M^{2+}-substituted end members of meridianiite have been synthesised, even by extreme disequilibrium methods [19,20]. However, substantial uptake of dopant cations by the meridianiite structure, exceeding 50 mol. %, was found for Co^{2+} and Mn^{2+} when aqueous solutions were flash frozen. This contrasts with the

* Corresponding author. Current permanent address, ISIS Facility, STFC Rutherford Appleton Laboratory, Harwell Science and Innovation Campus, Chilton, Didcot, Oxfordshire, OX11 0QX, UK.
E-mail address: dominic.fortes@stfc.ac.uk (A.D. Fortes).

behaviour of Ni^{2+}, Zn^{2+} and Fe^{2+} where limited substitution (<30 mol. %) was observed and a sequence of novel lower hydrates, with $n = 8$ and 9, were seen instead. It is therefore of some interest to characterise the *equilibrium* behaviour of systems that show the largest degree of substitution into the meridianiite structure on flash freezing, namely Co^{2+} and Mn^{2+}.

$MgSO_4 \cdot 11H_2O$ occurs naturally in various glacial and periglacial environments [63,28]: and in a limited number of $MgSO_4$-rich hypersaline lakes during the winter months [56,5]. On Mars, abundant Mg^{2+}- and Fe^{3+}-sulfates are known to occur and it has been hypothesized that meridianiite may be present in a permafrost-like deposit, forming a substantial reservoir of bound water in the near-surface regolith [14,15,55]. Where conditions are sufficiently oxidising and natural concentrations of transition metals occur in ore bodies then Co^{2+} and Mn^{2+} might also be a component of martian brines. Until relatively recently, such oxidising conditions were believed not to have prevailed on early Mars, but the detection by the Mars Science Laboratory (Curiosity rover) of >25 wt % Mn-oxides in fracture-filling materials at Gale crater, Mars, has altered that view [46,47]. Hence the occurrence of manganoan or cobaltoan meridianiite on Mars should be recognised as a possibility.

Similarly, water-rock interactions during the accretion and differentiation of icy planetary bodies in the outer solar system may have resulted in large brine reservoirs crystallising substantial quantities of $MgSO_4$ and Na_2SO_4 cryohydrates [41]. The partitioning of 'trace' elements into water-rich hydrates such as meridianiite therefore has mineralogical and planetary significance and allows inferences to be made about the composition of subsurface brine reservoirs by examination of salt hydrates deposited on a planet's surface.

There are more Earth-bound ramifications in relation to mine-wastes for substantial uptake of heavy metals in meridianiite. Increasing exploitation of ore deposits, particularly at high northern latitudes in Canada, Greenland and Russia, is likely to result in the formation of heavy-metal bearing cryohydrates as secondary minerals from mine-water waste, processing waste and effluent. We know from prior work [17,16]: that hexavalent chromium and selenium are readily taken up in meridianiite-structured crystals at temperatures down to 258 K. This work shows that meridianiite has the potential to apply a seasonal control on the mobilization of heavy elements as meridianiite forms in the winter and undergoes partial melting in the spring. Similar phenomena are recognized in temperate climates where spring rainfall dissolves secondary sulfate minerals, thereby increasing the metal load in surface run-off (see Ref. [30] and references therein).

Recognising and quantifying the uptake and storage of heavy metals, including divalent Co and Mn and hexavalent Cr and Se, in cryohydrates represents a significant step towards mitigating the environmental hazard posed by exploiting their ores in cold environments. It has recently been observed that knowledge of the thermodynamic properties of mine-drainage sulfates is lacking [51], and the absence of hitherto unknown or uncharacterised cryohydrates in aqueous geochemical models (see, e.g., Ref. [50]) exacerbates that knowledge gap.

Finally, the uptake of impurities in cryohydrates has technological relevance with the emergence of 'Eutectic Freeze Crystallisation' (EFC) as an energy-efficient method of water purification [60]. There have been several EFC-related studies involving low-temperature $MgSO_4$ brines (e.g., Refs. [34,27,35]) including work on the distribution of micro-impurities between liquid and crystal phases [26].

1.2. Scientific objectives

The system $MgSO_4-CoSO_4-H_2O$ was characterised previously between 298 and 313 K [2,53,52] and the system

$MgSO_4-MnSO_4-H_2O$ was studied between 273 and 373 K [33,4,75]. For the cobalt-doped system, low temperature data are lacking entirely, and for the manganese-doped system the 273 K isotherm pertains only to the two non-isotypic heptahydrates, orthorhombic $(Mg,Mn)SO_4 \cdot 7H_2O$ (Mn-bearing epsomite) and monoclinic $(Mn,Mg)SO_4 \cdot 7H_2O$ (Mg-bearing mallardite). Our main goals are therefore (*i*) to address the deficit in respect of the $MgSO_4-CoSO_4-H_2O$ system by characterising the crystal-liquid equilibria far below room temperature and (*ii*) to supplement existing work on the $MgSO_4-MnSO_4-H_2O$ system with data on the solubility of Mn-bearing meridianiite for comparison with 273 K data on Mn-bearing epsomite.

In addition to characterising the partitioning of dopants between solid and liquid, we also wish to identify any preference for occupancy of particular environments in the crystal. In $MgSO_4 \cdot 11H_2O$ (S.G. $P\bar{1}$, Z = 2) there are two symmetry-inequivalent octahedral sites (Fig. 1), the first on Wyckoff position $1a$ (0,0,0) and the second on Wyckoff position $1b$ (0,0,½); whilst the cations in these sites have very similar first nearest neighbour coordination shells, the more distant coordination and the pattern of hydrogen bonding differs considerably.

Using neutron single-crystal diffraction methods we can determine the complete structure, including the positions of all hydrogen atoms, to high precision and determine the relative occupancy of the $1a$ and $1b$ sites by different elements. In the case of Mg *vs* Mn the contrast in scattering lengths [66] is much greater for neutrons than for X-rays (5.38 *vs* −3.75 fm), giving far better site discrimination; for Mg *vs* Co the contrast is similar to that for X-rays, with the coherent scattering length differing by approximately a factor of two (5.38 *vs* 2.49 fm).

2. Experimental and computational method

2.1. Reagents

The materials used were all of analytical reagent grade, these being $MgSO_4 \cdot 7H_2O$ (Sigma-Aldrich M1880, ≥99.0%), $CoSO_4 \cdot 7H_2O$ (Sigma-Aldrich C6768, ≥99.0%) and $MnSO_4 \cdot H_2O$ (Sigma-Aldrich M7634, ≥99.0%). The solvent used was ACS reagent grade H_2O (Sigma-Aldrich 320072, $\sigma \leq 2$ S cm^{-1}).

2.2. Sample synthesis

$M^{2+}SO_4$ hydrates were weighed out and mixed together to form two sets of samples, one series from $MgSO_4$ to $CoSO_4$ in increments of 5 mol. % Co^{2+} up to 25 mol % and in 10% increments above 30 mol. %, and a second series from $MgSO_4$ to $MnSO_4$ in increments of 10 mol. % Mn^{2+}. These mixtures were then dissolved in H_2O to a concentration of 19 wt % (anhydrous basis) by gradually adding the coarsely-powdered solid mixtures to the liquid at ~ 320 K on a magnetic stirrer hotplate; when dissolution was complete the solutions were poured into polystyrene petri dishes (100 mm diam. × 11 mm deep). These dishes were transferred to a refrigerated room at a temperature of 270.1 (3) K, the air temperature adjacent to the samples being measured using a Tinytag Plus 2 cryogenic temperature recorder (Gemini Data Loggers TGP-4204), connected to a stainless-steel sheathed platinum resistance thermometer (Gemini PB-7002). Our goal was to achieve spontaneous nucleation on cooling into the stability field of the 11-hydrates, since we wished to minimise the induction time involved in evaporating the solution to saturation at low temperature; long periods of evaporation without agitation, even when comparatively slow, may result in the formation of metastable solutions and crystallisation of non-equilibrium phases. Certainly for the $CoSO_4$-bearing solutions and for the lightly doped $MnSO_4$ solutions this strategy worked well; nucleation
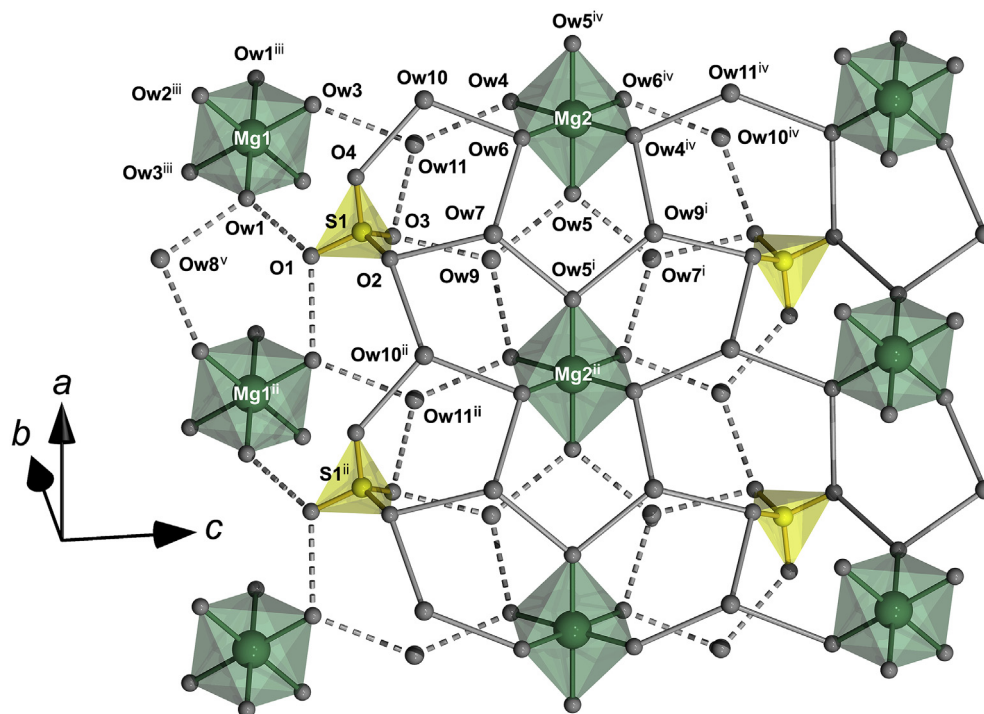
Fig. 1. Non H-atom framework connectivity in $MgSO_4 \cdot 11H_2O$, viewed approximately along b^*, showing the atom-labelling scheme used in this work. Dashed and solid lines are used to distinguish the hydrogen-bonded contacts between water oxygens and sulfate oxygens in different planes. Ow7 through Ow11 are interstitial water molecules, not coordinated to $Mg2+$. Note that the Mg1 octahedron donates H-bonds to the sulfate oxyanions whereas the Mg2 octahedron is exclusively involved with interstitial waters [Symmetry codes: (i) $-x + 1$, $-y$, $-z + 1$; (ii) $x - 1$, y, z; (iii) $-x + 2$, $-y$, $-z$; (iv) $-x + 2$, $-y$, $-z + 1$; (v) $-x + 1$, $-y$, $-z$]. Figure prepared with Crystal Impact's *Diamond* software [59].

occurred in ~1 day and all subsequent growth proceeded by slow isothermal evaporation. No attempt was made to control the air flow over the samples, to monitor the ambient humidity or to characterise the evaporation rates, and no subsequent efforts were made to identify or quantify any compositional zoning in the crystals which might result from variations in these environmental conditions. Nevertheless, we note that there was no evidence of colour-zoning in the strongly-coloured $CoSO_4$-bearing crystals and the compositional reproducibility between individual crystals and between batches of crystals was very good; this indicates to us that the evaporation rates were conducive to equilibrium growth. Once a satisfactory population of crystals had developed, further evaporation was halted by covering the petri dishes, after which the crystals were left for approximately three weeks with occasional agitation before extraction. In all but the more Mn-rich solutions, crystals nucleated and grew to horizontal dimensions greater than 1 cm over a period of several days (Fig. 2). Crystals were ultimately separated from their mother liquor and dried on filter paper. Gentle drying is essential with these low melting-point materials in order to avoid decomposition by body heat or else by the application of vacuum suction methods. Samples of the residual liquids were stored in glass vials at ~295 K and the crystals were stored in a freezer at 255 K. Solutions containing <50 mol. % Mn^{2+} produced only undecahydrate crystals whereas solutions containing >50 mol. % Mn^{2+} produced no crystals for the duration of the experiment. We are therefore unable to present data pertaining to $(Mg,Mn)SO_4 \cdot 7H_2O$ solid solutions or solid-liquid equilibria; since these were already reported by Ref. [4] at 273 K, there is no significant loss.

2.3. Analysis

The water content was determined by drying of liquid and crystalline materials in a furnace at 673 K for a minimum of 72 h, conditions demonstrated repeatedly to result in complete loss of
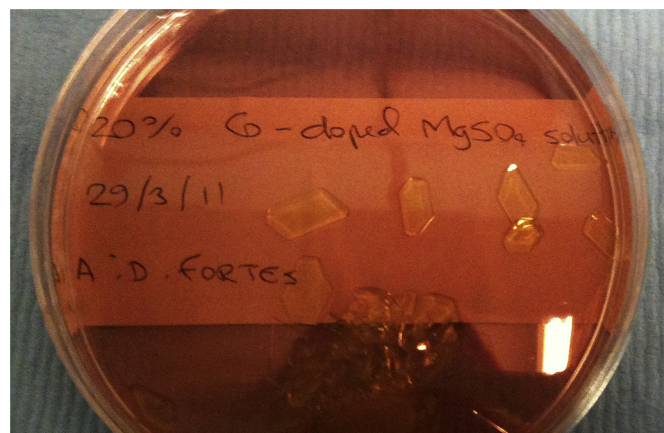
Fig. 2. Overview of a typical batch of Co-doped meridianiite crystals growing from their parent solution in a 100 mm diameter petri dish at 270 K.

water from these materials [8,69,70,13,49,23]. Samples were decanted into 10 mL Pyrex beakers and weighed before and after thermal treatment. The composition of co-existing solids and liquids was determined by re-dissolving the powder residue obtained after heating in ultra-pure water ($\sigma = 0.055$ μS cm^{-1}) to a concentration in the region of a few 10s of mg L^{-1}; inductively coupled plasma optical emission spectroscopy (ICP-OES) carried out with a Horiba JY Ultima 2C was then used to analyse the liquid for Mg, Mn and Co. Numerous separate solid and liquid aliquots of each composition were analysed between two and four times to assess reproducibility, as reported in Table 1.

Given the difficulty of adequately drying the surfaces of crystals and of obtaining crystals entirely free of mother liquor in blebs or stringers in their interiors, the solids were treated as 'wet residue'

Table 1
Composition of co-existing liquid and solid phases (wt %), mole fraction of the dopant cation in each and the hydration state of the equilibrium crystalline phase: '11' = triclinic meridianiite-structured undecahydrate; '7' = monoclinic bieberite-structured heptahydrate.

Sample ID	Liquid composition (wt %)		Wet crystalline residue (wt %)		Calculated dry residue (wt %)		Mole fraction of M^{2+} in liquid[a]	Mole fraction of M^{2+} in solid[a]	Solid phase
	$MgSO_4$	$CoSO_4$	$MgSO_4$	$CoSO_4$	$MgSO_4$	$CoSO_4$	M^{2+} = Co	M^{2+} = Co	
Co_5	17.14 (8)	1.20 (7)	35.0 (2)	2.2 (2)	35.82	2.29	0.0528	0.0485	11
Co_10a	16.07 (7)	2.32 (7)	33.1 (2)	4.3 (2)	33.97	4.44	0.1009	0.0922	11
Co_10 b	15.93 (7)	2.51 (7)	32.7 (2)	4.6 (2)	33.68	4.77	0.1116	0.1014	11
Co_15	15.23 (8)	3.74 (8)	31.2 (2)	6.6 (2)	31.99	6.73	0.1638	0.1436	11
Co_20a	14.40 (8)	4.85 (8)	29.7 (2)	8.5 (2)	30.33	8.67	0.2072	0.1816	11
Co_20 b	14.49 (8)	4.75 (8)	29.5 (2)	8.8 (2)	30.09	8.95	0.2030	0.1876	11
Co_20c	14.59 (8)	4.65 (8)	29.7 (2)	8.5 (2)	30.32	8.68	0.1984	0.1819	11
Co_20 d	14.04 (8)	5.13 (8)	30.0 (2)	8.8 (2)	30.18	8.84	0.2256	0.1892	11
Co_25	13.40 (8)	6.29 (8)	28.7 (2)	10.8 (2)	28.52	10.76	0.2722	0.2312	11
Co_30	12.71 (8)	7.31 (7)	26.7 (2)	12.5 (2)	26.92	12.62	0.3088	0.2669	11
Co_40	10.87 (8)	9.91 (8)	23.9 (2)	16.1 (2)	23.92	16.11	0.4145	0.3434	11
Co_50a	9.06 (8)	12.43 (8)	20.1 (1)	20.4 (1)	20.17	20.46	0.5158	0.4406	11
Co_50 b	8.53 (7)	12.14 (7)	22.4 (2)	18.2 (2)	22.22	18.09	0.5317	0.3935	11
Co_60a	8.04 (8)	13.25 (8)	10.0 (2)	42.8 (2)	10.07	43.79	0.5613	0.7716	7
Co_60 b	10.19 (8)	12.77 (8)	11.9 (2)	40.1 (2)	11.85	41.78	0.4931	0.7325	7
Co_70	6.62 (8)	14.95 (8)	7.0 (2)	46.0 (2)	7.00	47.26	0.6367	0.8398	7
Co_80a	5.06 (7)	16.19 (7)	4.7 (2)	49.2 (2)	4.66	49.90	0.7131	0.8926	7
Co_80 b	5.00 (7)	16.25 (7)	5.0 (2)	48.9 (2)	4.98	49.54	0.7163	0.8854	7
Co_80c	4.93 (7)	16.31 (7)	4.7 (2)	49.1 (2)	4.74	49.81	0.7197	0.8908	7
Co_90	2.82 (7)	18.48 (7)	2.5 (2)	51.3 (2)	2.46	52.38	0.8357	0.9430	7
Co_100	0.03 (6)	18.70 (6)	0.0 (2)	53.1 (2)	–	–	–	–	7
	$MgSO_4$	$MnSO_4$	$MgSO_4$	$MnSO_4$	$MgSO_4$	$MnSO_4$	M^{2+} = Mn	M^{2+} = Mn	
Mn_10	17.14 (7)	3.01 (8)	34.9 (1)	1.6 (1)	36.48	1.50	0.1228	0.0316	11
Mn_20a	15.63 (9)	6.82 (9)	33.4 (1)	3.8 (1)	34.68	3.56	0.2580	0.0757	11
Mn_20 b	15.65 (9)	6.80 (9)	33.4 (1)	3.8 (1)	34.65	3.60	0.2573	0.0764	11
Mn_20c	15.68 (9)	6.78 (9)	33.3 (1)	3.9 (1)	34.58	3.68	0.2564	0.0781	11
Mn_25	14.43 (8)	8.11 (8)	33.3 (1)	4.6 (1)	33.86	4.49	0.3094	0.0956	11
Mn_30	14.99 (9)	9.94 (9)	30.1 (1)	7.0 (1)	32.05	6.57	0.3457	0.1405	11
Mn_50a	10.4 (1)	17.9 (1)	28.7 (2)	10.6 (2)	28.47	10.67	0.5801	0.2301	11
Mn_50 b	10.2 (1)	18.1 (1)	28.5 (2)	10.8 (2)	28.27	10.90	0.5844	0.2350	11
Mn_50c	10.4 (1)	17.9 (1)	28.5 (2)	10.7 (2)	28.33	10.83	0.5786	0.2335	11

[a] Calculated using the molar masses of $MgSO_4$ = 120.3676 g mol^{-1}, $CoSO_4$ = 154.9958 g mol^{-1} and $MnSO_4$ = 151.006 g mol^{-1}.

and the compositions corrected using Schreinemakers' Method [65,64,6], even though this correction typically was small, as can be seen in Figs. 5 and 7.

## 2.4. Crystalline phase identification

Both the hepta- and undecahydrates have distinctive crystal habits and, in the case of the Co-bearing species, colour. The
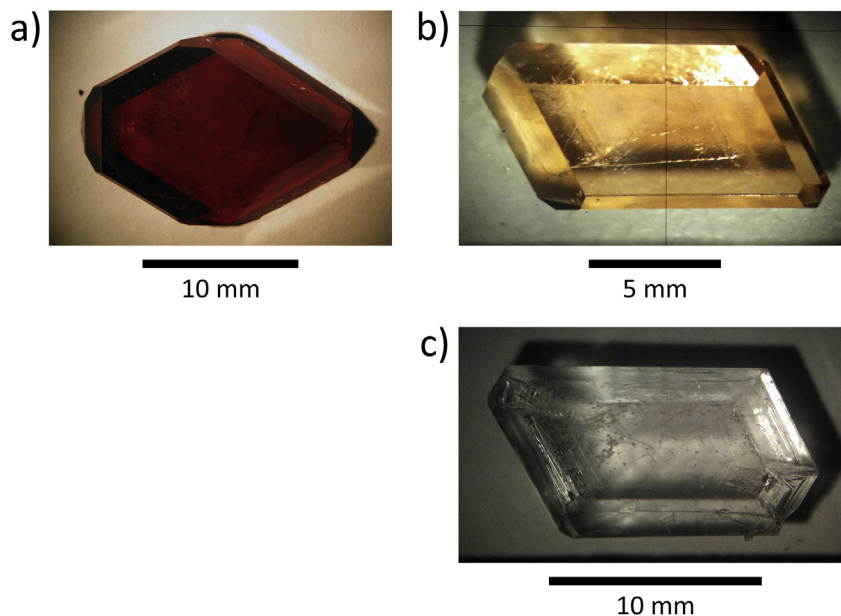

Fig. 3. Representative photographs of heptahydrate (a) and undecahydrate (b,c) single crystals produced in this work.

a)

b)
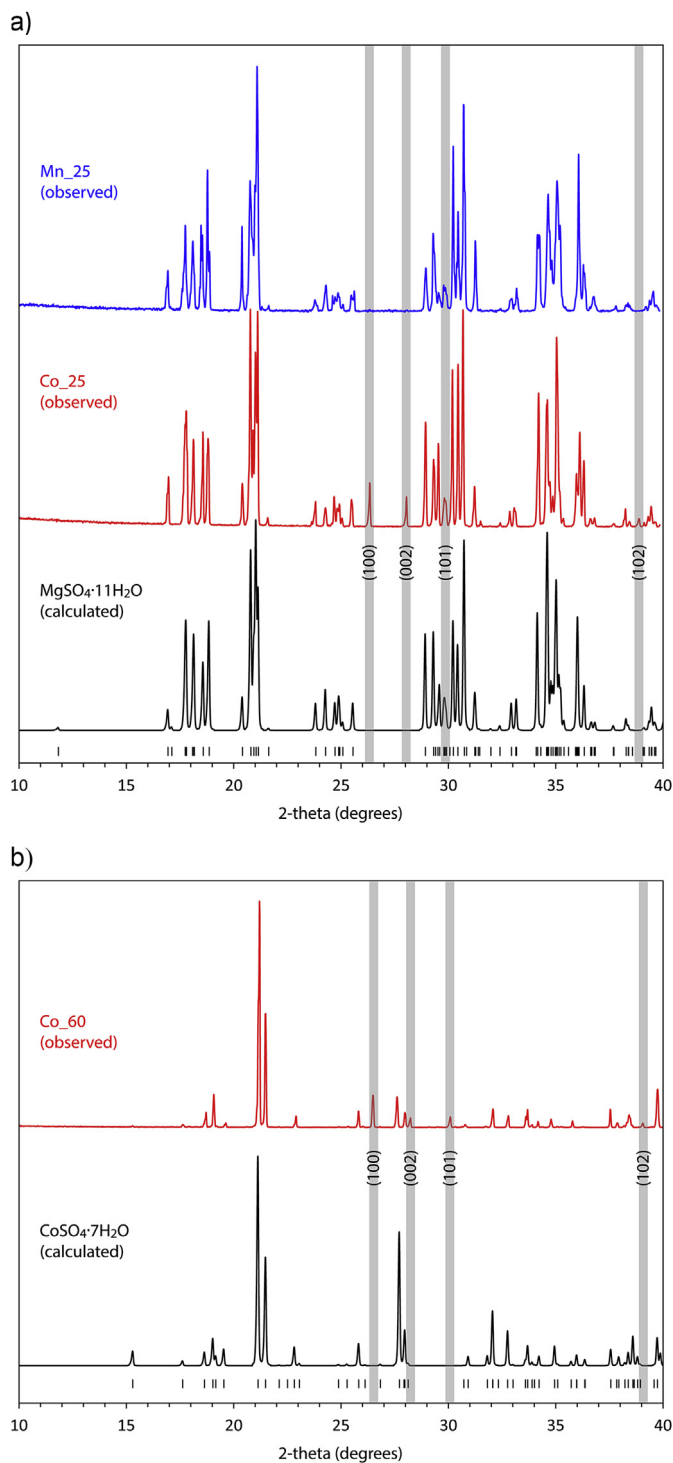
Fig. 4. Representative X-ray powder diffraction patterns of (a) $M^{2+}SO_4 \cdot 11H_2O$ crystals compared with the calculated diffraction pattern of an ideal $MgSO_4 \cdot 11H_2O$ end-member, and (b) $M^{2+}SO_4 \cdot 7H_2O$ crystals compared with the calculated diffraction pattern of an ideal $CoSO_4 \cdot 7H_2O$ end-member. Some samples contain small amounts of water ice, which is derived either from freezing of mother liquor trapped in the crystals or from condensation of ice onto the powder samples during preparation; the positions of Bragg peaks from water ice are indicated by the grey vertical bars. Other differences between the real and calculated diffraction patterns are due to shifts in cell parameters by virtue of the chemical substitution and often substantial amounts of preferred orientation from preparation of a pressed powder specimen using quite coarsely-powdered single crystal fragments.
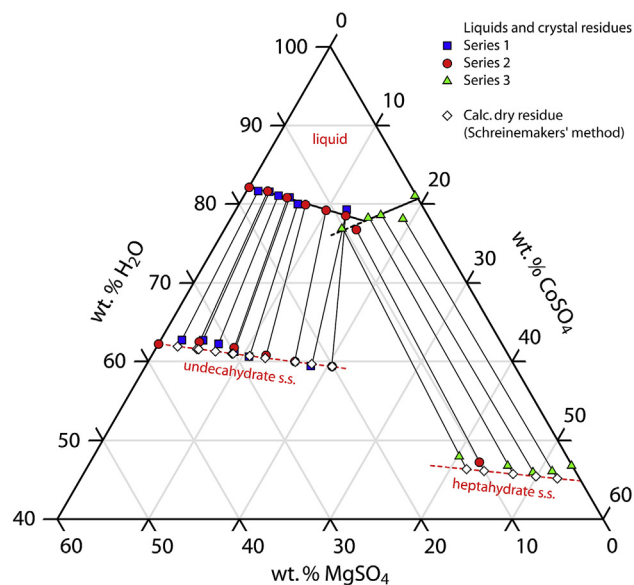
Fig. 5. Ternary solubility diagram at 270 K at the water-rich end of the system $MgSO_4-CoSO_4-H_2O$. Plotted with ProSim Ternary Diagram 1.0 (http://www.prosim. net).
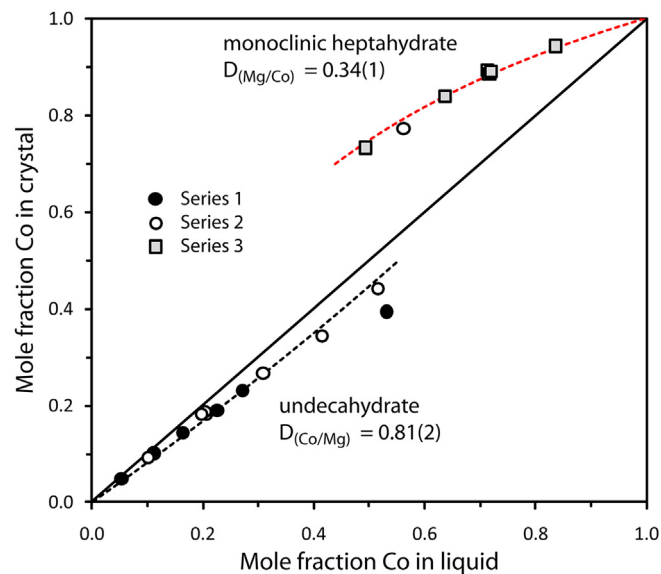
Fig. 6. Measured partitioning of cobalt between liquid and meridianiite and of magnesium between liquid and bieberite at 270 K; dashed lines report the best fit distribution coefficients obtained by unweighted least-squares fitting in Origin Pro.

monoclinic heptahydrate of $CoSO_4$ forms dark red platy crystals with a spade-like shape (Fig. 3a) whilst the triclinic Co-bearing undecahydrates are a lucent orange colour and usually adopt an inclined rhombus-like shape (Fig. 3b). The $MnSO_4$-bearing undecahydrates are all virtually colourless and share the same inclined rhombic outline as other meridianiite-structured crystals (Fig. 3c). On the whole, Co-bearing meridianiite crystals are blockier and the Mn-bearing analogues form thinner plates.

Despite the obvious morphological differences, supporting X-ray powder diffraction data were collected to confirm phase identity. These data were acquired with a PANalytical X'Pert Pro

multipurpose powder diffractometer (with Ge-monochromated Co Kα_1 radiation and X'Celerator multi-strip detector) using a thermoelectrically cooled cold stage [73]. Powder diffraction patterns were measured in the range of 5–90° 2θ at 250 K and compared with data obtained previously from end-member $MgSO_4 \cdot 11H_2O$, $CoSO_4 \cdot 7H_2O$ and solid solutions formed by quenching of aqueous solutions in liquid nitrogen (see Refs. [19,20]). The X-ray powder diffraction data supported the clear morphological distinction between triclinic 11-hydrate and monoclinic 7-hydrate crystals (Fig. 4).

2.5. Time-of-flight neutron single-crystal diffraction

Two sets of experiments were carried out using the SXD time-of-flight Laue diffractometer at the ISIS neutron spallation source [29,42]. Firstly, crystals grown from liquids with initial dopant concentrations of 25 and 50 mol. % Co and Mn were studied at 250 K. Raw uncut crystals similar to those shown in Figs. 2 and 3, with masses between 50 and 350 mg, were loaded into thin-walled vanadium tubes in UCL Earth Sciences' refrigerated laboratory and transported to ISIS packed in dry ice; for each analysis a pair of crystals was used in order to maximise the number and reciprocal-space coverage of measured reflections. Sample tubes were loaded into a closed-cycle refrigerator (CCR) on the SXD beamline and equilibrated at 250 K. Frames of data were then obtained at a series of six discrete angular positions about the vertical axis over a period of 15–23 h depending on counting statistics.

Subsequently, further measurements were made at 10 K on a fresh set of crystals grown from solutions doped with 50 mol. % Co and Mn. These were cut with a scalpel blade into crude cubes of approximate dimensions 2 × 2 × 2 mm and loaded (again, in pairs) into thin-walled vanadium cans. The measurement strategy for these crystals was the same as the first batch. The opportunity to carry out this second set of measurements at low temperatures offered a number of benefits: firstly, at low temperature were able to measure substantially more reflections; secondly, the smaller and more equant crystals led to a smaller and more easily-applied absorption correction; finally, we could establish the reproducibility of the site occupancies, using new crystals measured under different conditions at a different time. The overall effect of this was to significantly improve the model fit, R (F^2), compared with the previous measurements and to reassure us that the site occupancies were meaningful.

The time-of-flight Laue peaks were integrated using the SXD2001 program and exported as hkl versus intensity files suitable for analysis with the GSAS/Expgui package [48,72].

2.6. Density functional theory calculations

In an effort to understand the effect of substituting Co and Mn on different sites in the meridianiite structure, we carried out a series of first-principles calculations using Density Functional Theory, DFT, and the plane-wave pseudopotential method [37,43]. The calculations were carried out using CASTEP [54,67,9] in conjunction with the analysis tools in the Materials Studio software package (http://accelrys.com). Tests for convergence of the total energy and of structural parameters were done by varying the basis-set cut-offs and the reciprocal-space sampling. We found that the Wu–Cohen GGA functional [74] gives more accurate structural parameters than PBE for these materials, reducing the ~5% over-estimation of molar volume to a ~1% under-estimation. Total energy and strain convergence of 1 meV per atom and 0.01 GPa, respectively, was achieved with a basis-set cut-off of 1200 eV and a 4 × 4 × 2 k-point grid, corresponding approximately with a reciprocal lattice spacing of 4 × 4 × 3 × 10^{-2} Å^{-1}.

Spin-polarized calculations were done for the transition metal-bearing compounds so as to allow degenerate d-orbitals to adopt differing energy levels. Lastly, as is well-known, DFT does not properly treat the Coulomb interactions of highly localised d and f electrons in transition metal elements [38]. A correction of the on-site Coulomb interaction (U) and the on-site exchange interaction (J) to the Hohenberg-Kohn-Sham Hamiltonian is achieved by the use of a Hubbard interaction parameter. The CASTEP implementation adopts the $U_{eff} = U - J$ approach of [12] and we use literature values of $U_{eff} = 4.40$ eV for Co [7] and $U_{eff} = 3.75$ eV for Mn [76].

Structural relaxations under zero-pressure athermal conditions were carried out using the Broyden-Fletcher-Goldfarb-Shanno method [57]. The relaxations were considered to have converged when the forces on each atom were less than 1 × 10^{-2} eV Å^{-1} and each component of the stress tensor was smaller than 0.01 GPa.

A baseline structural relaxation was done on pure Mg-meridianiite and on crystals containing 50 atom % Co or Mn. The cation-doped calculations were done with the dopant entirely occupying the 1a site (with Mg on the 1b site) and then with the dopant entirely filling the 1b site (and Mg on 1a). Calculations involving lower dopant concentrations or more elaborate site distribution models would involve the use of large supercells; given the computational expense of running these calculations, particularly for spin-polarized systems, such models were not explored here.

3. Results

The composition of co-existing liquid and solid phases at 270 K (both original 'wet' residue and calculated 'dry' values) are listed in Table 1 and depicted graphically on ternary phase diagrams in Fig. 5 (for Co-doping) and Fig. 7 (for Mn-doping). The delineation of experimental points into different series indicates results from separate batches of freshly-prepared parent solutions each of which underwent crystallisation in consecutive three-week periods. Hence the level of agreement between independent series is a good reflection of how reproducible the measurements of solubility were.

### 3.1. Solid-liquid equilibria in the $MgSO_4$–$CoSO_4$–H_2O system at 270 K

At 270 K we observe two solid-solution series, one involving Co-bearing $MgSO_4 \cdot 11H_2O$ and the other involving Mg-bearing $CoSO_4 \cdot 7H_2O$, with a miscibility gap extending from ~47 mol % $CoSO_4$ to 77 mol % $CoSO_4$ (Fig. 6). The end-member solubilities at 270 K, either taken directly or found by extrapolation of literature data, are 18.1 wt % $MgSO_4$ at 270 K [58,35]: and 19.3 wt % $CoSO_4$ [71], which agree well with the values of 17.8 (1) wt % $MgSO_4$ and 18.8 (3) wt % $CoSO_4$ we obtain from our best-fit solubility curves.

There is a ternary eutonic point at 7.3 wt % $MgSO_4$, 14.8 wt % $CoSO_4$, 77.9 wt % H_2O. Clearly, a degree of metastability is possible on the Mg-rich side of the eutonic, with liquids becoming supersaturated with respect to the 11-hydrate solid solution and precipitating Mg-rich $CoSO_4 \cdot 7H_2O$ (dashed extension of the solubility curve). No similar behaviour is seen on the Co-rich side of the eutonic and no co-existence of the two hydrates was observed around the invariant point.

Intermediate hydration states with $n = 8$ and $n = 9$ are known to occur in flash frozen $MgSO_4$ solutions doped with Ni^{2+}, Zn^{2+} and Fe^{2+}. Similarly, a hitherto unknown Mg-selenate hydrate with $n = 9$ has been found recently to be stable in contact with aqueous solution [18]. These facts allow for the possibility that small regions of stability for hydration states intermediate between $n = 7$ and $n = 11$ might exist. However, we have seen no evidence for this at 270 K.
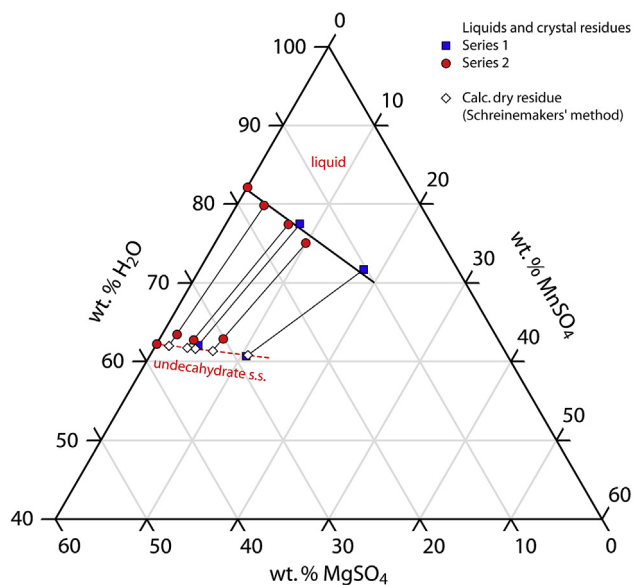
Fig. 7. Ternary solubility diagram at 270 K at the water-rich end of the system $MgSO_4-MnSO_4-H_2O$. Plotted with ProSim Ternary Diagram 1.0 (http://www.prosim.net).
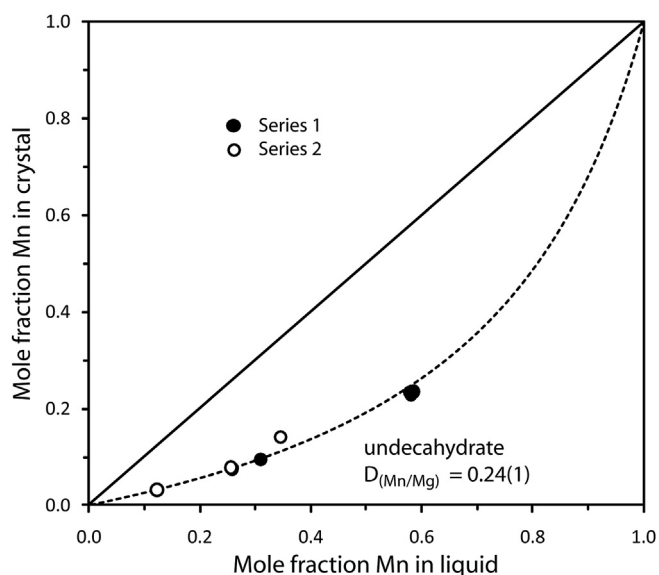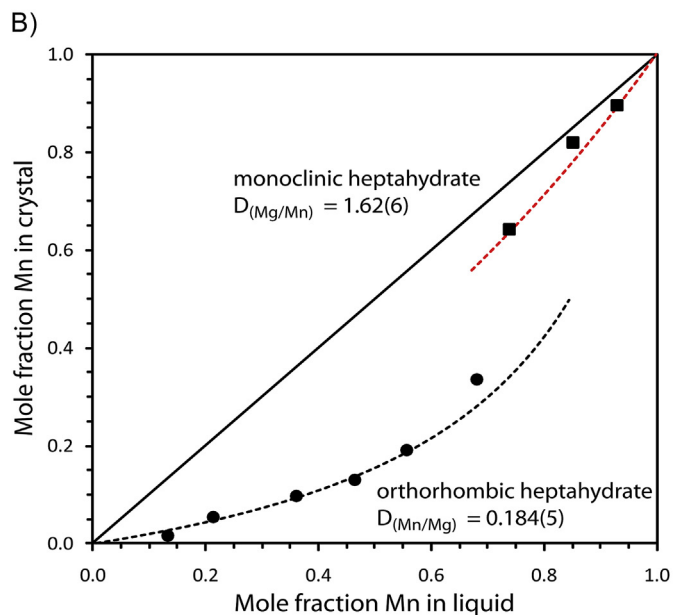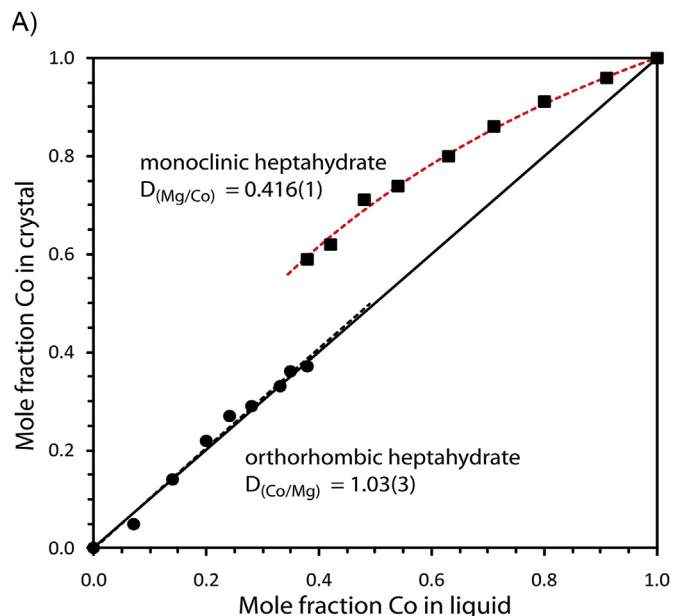

Fig. 8. Measured partitioning of manganese between liquid and meridianiite at 270 K; the dashed line shows the best-fitting distribution coefficient obtained by unweighted least-squares fitting in Origin Pro.

Fig. 9. (a) Partitioning of cobalt between liquid and two non-isotypic heptahydrate crystals at 298 K [2]: (b) Partitioning of manganese between liquid and two non-isotypic heptahydrate crystals at 273 K [4]. As before, symbols are measured values and dashed lines are least-squares fits of distribution coefficients that we have done.

The partitioning of Co between the liquid and solid phase is drawn in Fig. 6; the solid diagonal line represents a uniform distribution of the dopant cation between solution and crystal and dashed lines show best-fit values of constant distribution coefficients, D, such as one would expect for the partitioning of macro amounts of dopant in an ideal solid solution. The partition coefficient is defined as (for example):

$$D_{(Co/Mg)} = \left(\frac{Co}{Mg}\right)_S \bigg/ \left(\frac{Co}{Mg}\right)_L$$

where the subscripts S and L denote mole fractions in the solid and liquid phases, respectively. Evidently, meridianiite has a greater

preference for cobalt, $D = 0.81$ (2), than bieberite does for magnesium, $D = 0.34$ (1).[1]

3.2. Solid-liquid equilibria in the $MgSO_4-MnSO_4-H_2O$ system at 270 K

At 270 K we observed only a single solid-solution series involving Mn-bearing $MgSO_4 \cdot 11H_2O$ (Figs. 7 and 8). The lack of

---

[1] Since this is a two-component system, we can write $(Mg)_S = 1 - (Co)_S$ and $(Mg)_L = 1 - (Co)_L$. Substituting these into the expression for the distribution coefficient leads to the equation used for least-squares determination of D. $(Co)_S = \left[\frac{1}{D}\left(\frac{1}{(Co)_L} - 1\right) + 1\right]^{-1}$.

crystallisation from more Mn-rich liquid over the three-week duration of the experiments is likely to reflect the much higher solubility of $MnSO_4$ (34 wt % at 273 K: Ref. [10]), thus requiring more time to reach saturation from the 19 wt % initial composition, and the substantial increase in viscosity of the concentrated solution [11]. After three weeks open to the air, $MnSO_4$-bearing solutions exhibited signs of oxidation in the form of a thin film of brown MnO_2 deposited on the bottom of the petri dish. The significance of this is considered to be negligible since the oxidation occurred after lengthy exposure to air, when virtually all crystal growth was complete. Moreover, the oxide film was very thin, being apparent only when the liquid was agitated. In the more Mn-rich solutions where crystallisation had not occurred after three weeks, the presence of this oxidation film led us to dispose of the liquid rather than wait longer for nucleation to occur.

The end-member solubility derived by a quadratic fit to the liquid compositional data is 17.9 (8) wt % $MgSO_4$, which is in agreement with (if less well determined than) the value found in the $MgSO_4-CoSO_4-H_2O$ ternary system.

The partitioning of Mn between the liquid and solid phase is drawn in Fig. 8; meridianiite clearly has a lesser affinity for manganese, D = 0.24 (1) than for cobalt, which may be attributable to the greater ionic radius of octahedrally coordinated high-spin Mn^{2+}, 0.83 Å, compared with Mg^{2+}, 0.72 Å, and high-spin Co^{2+}, 0.74 Å [68].

3.3. Comparisons with solubility data obtained at higher temperatures

Fig. 9 shows element partitioning data for Co/Mg at 298 K [2] and for Mn/Mg at 273 K [4]. Cobalt is uniformly distributed between orthorhombic $MgSO_4 \cdot 7H_2O$ and the co-existing liquid, with $D_{(Co/Mg)} = 1.03$ (3). Conversely, the uptake of Mg into monoclinic $CoSO_4 \cdot 7H_2O$ is less efficient, with $D_{(Mg/Co)} = 0.416$ (1). Oikova & Barkov [52] made measurements at 313 K from which we obtain $D_{(Mg/Co)}$ in bieberite equal to 0.51 (2); clearly the structure is able to accommodate Mg more readily at higher temperatures. Indeed, from these two data points and our own at 270 K, we find an unweighted linear increase of $D_{(Mg/Co)} = 0.004$ (1) K^{-1} on warming from 270 to 313 K.

Fig. 9b shows that the $D_{(Mn/Mg)}$ for both meridianiite and epsomite are similar to 0.2, reflecting the difficulty in accommodating the much larger Mn^{2+} ion into both of these structures.

3.4. Site partitioning in the undecahydrate crystal structure

Structural refinements of the single-crystal neutron diffraction data using GSAS/Expgui yield bulk stoichiometries in good agreement with values obtained by ICP-OES, albeit with much larger uncertainties (Table 2). Note that the errors on the site occupancies and the propagated errors on bulk composition and site partitioning are larger for the Co-doped crystals by virtue of cobalt's smaller neutron scattering contrast with Mg than manganese. One of the most important aspects of these structural refinements is the striking difference in site preference between the two dopant cations: cobalt shows a clear preference for the 1b site (0,0,½) and manganese, conversely, prefers to a lesser degree to occupy the 1a site (0,0,0). This observation is reproducible in crystals of different dopant concentrations and in independent batches of crystals of a given concentration measured at different times and under different conditions.

The observation is difficult to explain in terms of the dimensions of the respective coordination polyhedra, as is commonly the case in polyhedral framework compounds. For example, olivine consists of a quite rigid array of approximately hexagonal close-packed oxygen atoms, which define one tetrahedral cavity and two types of octahedral cavities, M1 and M2. In forsterite olivine (Mg_2SiO_4), the M2 site is ~5% larger and is more distorted than the M1 site, the consequence of which is that there are strong site preferences for dopant cations based on ionic radius. The larger Mn^{2+} ion is strongly partitioned onto the larger M2 site in forsterite [1,61]: whilst the smaller Co^{2+} ion prefers the smaller M1 site [45]. In meridianiite there is no close-packed oxygen framework, but instead a much looser hydrogen-bonded network in which the coordination polyhedra are embedded. From single-crystal neutron diffraction analysis we know to high precision that the two

Table 2
Results of single-crystal neutron diffraction analysis of Co- and Mn-doped meridianiite crystals. The upper portion of the table reports details of each dataset and the model fit quality; the lower portion of the table shows refined cation site occupancies. Complete structural information is in the supplementary electronic data.

	Co-bearing $MgSO_4 \cdot 11H_2O$			Mn-bearing $MgSO_4 \cdot 11H_2O$		
	Co25	Co50_1	Co50_2	Mn25	Mn50_1	Mn50_2
Measurement T (K)	250	250	10	250	250	10
Reflections	4065	4869	7364	4871	3667	9237
$I > 3\sigma(I)$						
h	$-9 \rightarrow 10$	$-12 \rightarrow 20$	$-16 \rightarrow 15$	$-9 \rightarrow 11$	$-6 \rightarrow 11$	$-17 \rightarrow 17$
k	$-17 \rightarrow 16$	$-11 \rightarrow 23$	$-13 \rightarrow 10$	$-16 \rightarrow 12$	$-9 \rightarrow 13$	$-18 \rightarrow 15$
l	$-37 \rightarrow 35$	$-28 \rightarrow 47$	$-41 \rightarrow 37$	$-25 \rightarrow 31$	$-28 \rightarrow 25$	$-44 \rightarrow 39$
d-spacing min (Å)	0.371	0.258	0.362	0.360	0.507	0.358
d-spacing max (Å)	6.034	6.049	17.353	8.636	6.050	6.004
R (F^2)	0.200	0.214	0.172	0.206	0.219	0.137
R(F)	0.108	0.115	0.092	0.113	0.116	0.078
Site occupancies						
Mg on 1a site (0,0,0)	0.97 (5)	0.78 (4)	0.82 (3)	0.86 (1)	0.73 (2)	0.677 (7)
M^{2+} on 1a site (0,0,0)	0.03 (5)	0.22 (4)	0.18 (3)	0.14 (1)	0.27 (2)	0.323 (7)
Mg on 1b site (0,0,½)	0.64 (5)	0.38 (4)	0.35 (3)	0.94 (1)	0.84 (2)	0.848 (7)
M^{2+} on 1b site (0,0,½)	0.36 (5)	0.62 (4)	0.65 (3)	0.06 (1)	0.16 (2)	0.152 (7)
Partition coeff., K_D[a]	**0.05(9)**	**0.17(4)**	**0.12(2)**	**2.6(5)**	**1.9(3)**	**2.7(1)**
Bulk composition (M^{2+} mol %)	20 (4)	42 (3)	42 (2)	10 (1)	21 (1)	23.8 (5)
ICP-OES (M^{2+} mol %)	22.9	42.5	42.5	9.9	22.7	22.7

[a] $K_D = [(M^{2+}/Mg)_{(1a)}]/[(M^{2+}/Mg)_{(1b)}]$ where M^{2+} is the mole fraction of the dopant cation (Co or Mn, respectively) and Mg is the mole fraction of Mg; the subscripts 1a and 1b indicate the two available crystallographic sites.
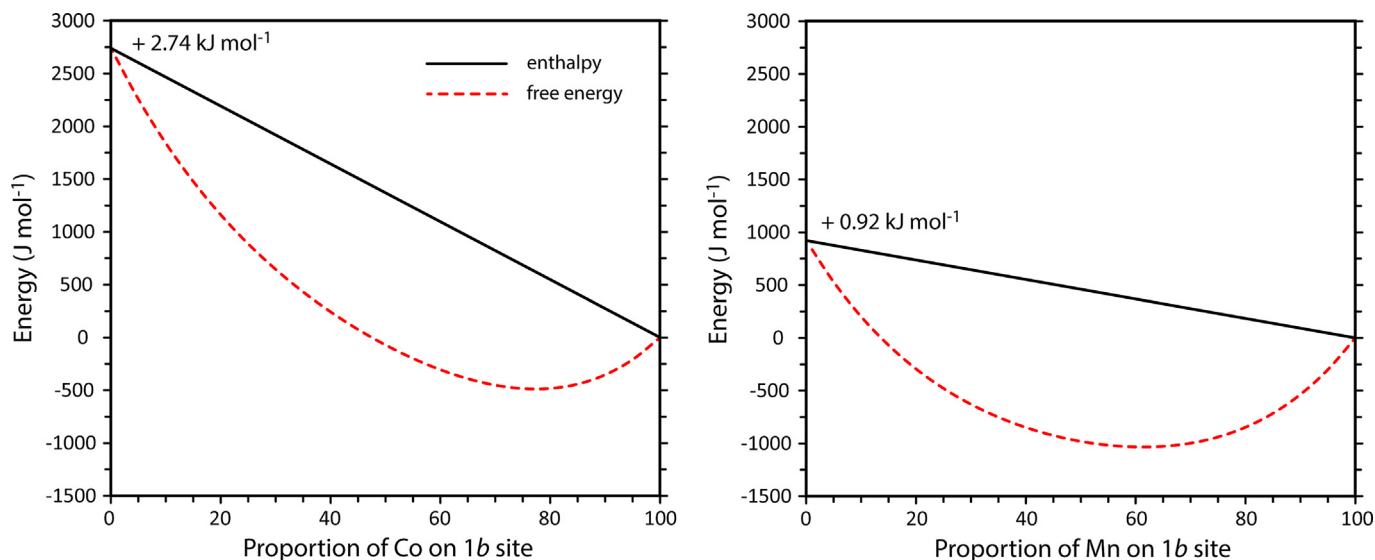
Fig. 10. For hypothetical meridianite crystals containing 50 atom % Co or Mn, the calculated variation of enthalpy at 0 K (solid black line) and free-energy at 250 K (dashed red line) as the *proportion* of dopant cobalt (a) or manganese (b) on the 1*b* site varies from 0 to 100%. (For interpretation of the references to colour in this figure legend, the reader is referred to the web version of this article.)

symmetry inequivalent Mg(H$_2$O)$_6$ octahedra in meridianiite differ in volume by just 0.1% and exhibit very similar degrees of bond length and bond angle variation [21]. The observed site partitioning in meridianiite must therefore be related to the way in which the structure beyond the first coordination sphere is able to accommodate larger or smaller cations or non-uniform distortion of the M(H$_2$O)$_6$ octahedra. It is therefore worth examining the wider differences in long-range coordination between these two sites. As illustrated by the structural connectivity map in Ref. [22] the Mg(H$_2$O)$_6$ octahedron centred on the 1*a* site donates three hydrogen bonds to interstitial water molecules, three hydrogen bonds to sulfate oxygens and accepts no hydrogen bonds. The Mg(H$_2$O)$_6$ octahedron centred on the 1*b* site donates six hydrogen bonds to interstitial water and accepts both arms of a bifurcated H-bond across one of the octahedral edges. Hence, the 1*a* site has a direct interaction with the sulfate group and the 1*b* site does not.

The most likely explanation is that there is a cation-dependent redistribution of charge outward to the ligand water molecules, which then influences the strength of hydrogen bonds to second-shell acceptors in a manner that depends on whether the acceptor oxygen is part of a water molecule or a sulfate anion. To a certain extent this is borne out by the results of DFT calculations reported in the next section.

3.5. DFT results

The most important initial observation pertains to the enthalpy, *H*, of the different doped structures. Whether doped with Co or with Mn, the models in which the dopant is located on the 1*b* sites each have the lowest enthalpy, although the enthalpic contrast is smaller for Mn by a factor of three. The model with Co on the 1*a* site is energetically disfavoured (at 0 K) by 2.74 kJ mol^{-1}, and that with Mn on the 1*a* site by 0.92 kJ mol^{-1}. The effect of temperature is introduced via the configurational entropy, S_{conf}, which for a lattice containing two inequivalent sites labelled M1 and M2 is described by:

$$S_{conf} = -R\left(v_{M1}\sum x_i^{M1}lnx_i^{M1}\right) - R\left(v_{M2}\sum x_i^{M2}lnx_i^{M2}\right)$$

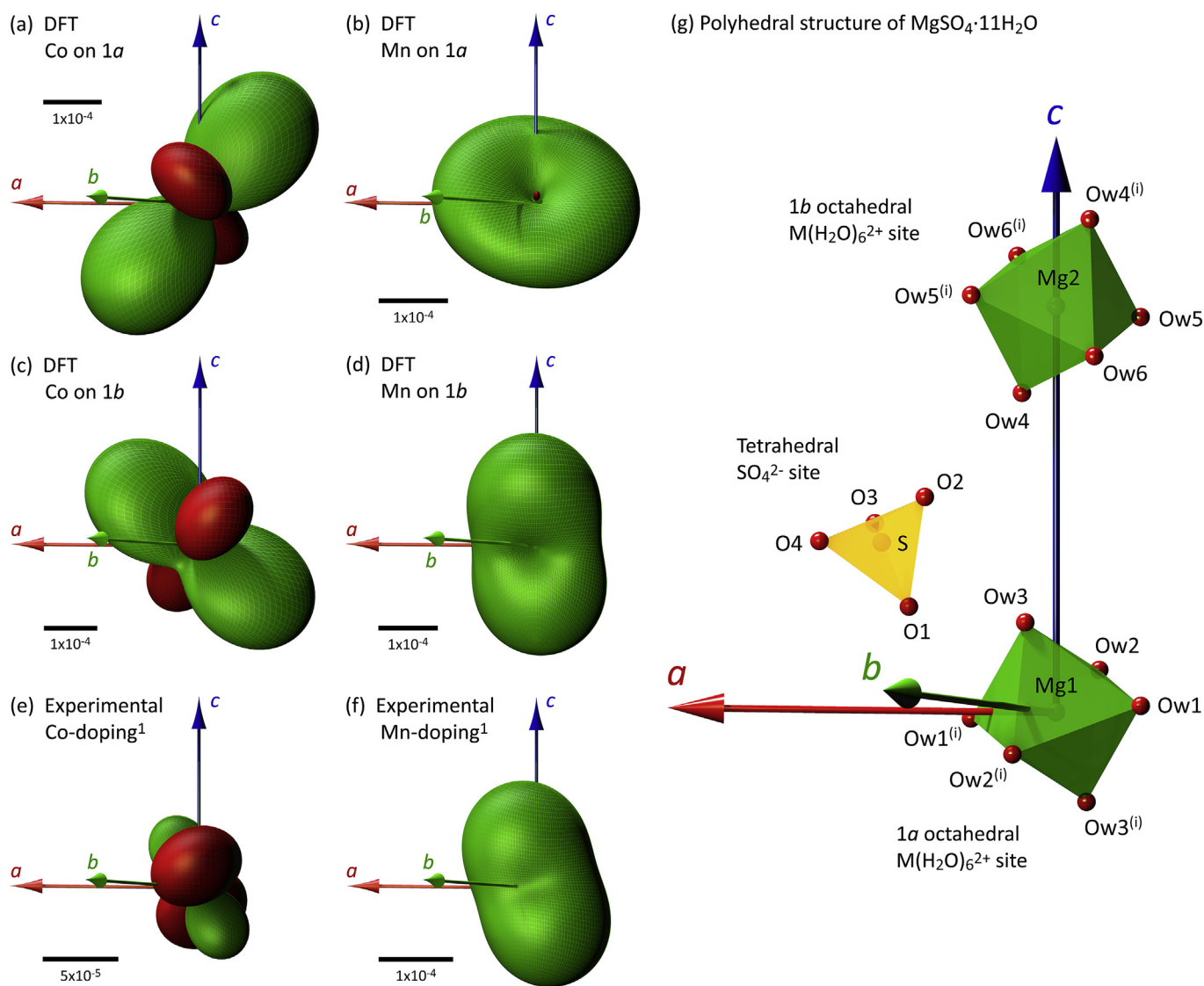where v_{M1} and v_{M2} are the number of moles of M1 and M2 sites per

formula unit and x_i^{M1}, for example, is the fractional occupancy of species *i* on the M1 site. For the case of site ordering where, for example, $x_{Co}^{1a} = 1$, $x_{Co}^{1b} = 0$, and site anti-ordering, where $x_{Co}^{1a} = 0$, $x_{Co}^{1b} = 1$, the total configurational entropy is zero. For the case of complete disorder across the two sites, S_{conf} reaches a maximum value of 5.762 J K^{-1} mol^{-1}.

Hence the difference in free-energy at finite temperature, $\Delta G = \Delta H - T\Delta S_{conf}$, will vary with site occupancy as shown by the dashed lines in Fig. 10, calculated for T = 250 K. For cobalt substitution, a minimum occurs when ~77% of the Co atoms are on the 1*b* site, which is essentially the same as we observe in the single-crystal refinements. For manganese substitution, the minimum occurs when ~61% of Mn atoms are on the 1*b* site, although the minimum is broad and quite flat from 55 to 65 atom % Mn on 1*b*. This differs somewhat from the single-crystal refinements where only 35% of Mn is found on 1*b*, with the majority on 1*a*. Nevertheless, the calculations support the overall experimental result that cobalt has a substantially greater preference for the 1*b* site than Mn and that Mn, whilst preferentially distributed, is rather more 'ambivalent' about its site occupancy.

Furthermore, the calculations allow us to evaluate in detail the response of the structure to the introduction of foreign cations. The Mg-pure meridianiite relaxation yields a unit-cell volume (Table 3) that is 0.9% smaller than the measured 4 K value [22], as expected for the Wu-Cohen GGA functional. The cation-doped structures each have larger molar volumes and substantially strained unit-cells. The effective Eulerian infinitesimal strain with respect to the Mg-pure structure was calculated using the method outlined by Ref. [32] and the unit-strain coefficients, ε_{ij}, are listed below the cell parameters in Table 3. The eigenvalues (the principal unit-strains, ε_i) are obtained by standard matrix decomposition methods and the volumetric strain, $\varepsilon_V = \varepsilon_1 + \varepsilon_2 + \varepsilon_3$. Since, for a crystal of triclinic symmetry, the principal directions need bear no relation to the crystallographic axes, a graphical depiction of the unit-strain tensor representation surface (Fig. 11) is a more useful way of illustrating the spatial relationships than a tabulated list of direction cosines (*cf.*, [31]). It is clear that the effect of cobalt substitution is very different from manganese substitution, producing large negative strains roughly perpendicular to the *a*−*c* plane (i.e., subparallel to *b**) and highly directional positive strains orthogonally. In contrast,

Table 3

Unit-cell parameters of Mg-pure meridianiite and hypothetical 50 atom % Co-doped and Mn-doped analogues as determined from DFT structural relaxations. Unit-strain tensor coefficients, and the eigenvalues of the strain tensor, are reported below.

	Pure Mg meridianiite	Co on 1a	Co on 1b	Mn on 1a	Mn on 1b
Unit-cell dimensions					
a (Å)	6.623307	6.660136	6.678814	6.672551	6.659671
b (Å)	6.807221	6.762641	6.776084	6.818661	6.824552
c (Å)	17.260227	17.382522	17.355476	17.346125	17.409940
α (°)	86.673270	87.479948	86.920667	86.983607	86.332583
β (°)	89.282351	90.002329	88.667891	89.238303	89.229527
γ (°)	63.441552	63.120247	62.807403	63.240772	63.392345
V (Å^3)	694.831813	697.473269	697.622758	703.667952	705.918013
Unit-strain tensor coefficients					
ε_{11}	–	11.28×10^{-5}	16.37×10^{-5}	14.85×10^{-5}	10.96×10^{-5}
ε_{22}	–	-17.70×10^{-5}	-19.20×10^{-5}	0.55×10^{-5}	3.46×10^{-5}
ε_{33}	–	14.17×10^{-5}	11.04×10^{-5}	9.95×10^{-5}	17.35×10^{-5}
ε_{12}	–	0.25×10^{-5}	4.14×10^{-5}	0.68×10^{-5}	-0.75×10^{-5}
ε_{13}	–	-12.66×10^{-5}	10.85×10^{-5}	0.81×10^{-5}	0.89×10^{-5}
ε_{23}	–	-10.20×10^{-5}	-10.89×10^{-5}	-6.68×10^{-5}	5.82×10^{-5}
Eigenvalues of unit-strain tensor					
ε_1	–	1.95×10^{-5}	25.18×10^{-5}	15.01×10^{-5}	11.02×10^{-5}
ε_2	–	-21.07×10^{-5}	-24.10×10^{-5}	-2.97×10^{-5}	1.24×10^{-5}
ε_3	–	26.87×10^{-5}	7.12×10^{-5}	13.32×10^{-5}	19.50×10^{-5}
ε_V	–	7.75×10^{-5}	8.21×10^{-5}	25.35×10^{-5}	31.77×10^{-5}

(a) DFT Co on 1a

(b) DFT Mn on 1a

(g) Polyhedral structure of MgSO$_4$·11H$_2$O

(c) DFT Co on 1b

(d) DFT Mn on 1b

(e) Experimental Co-doping[1]

(f) Experimental Mn-doping[1]

1b octahedral M(H$_2$O)$_6$$^{2+}$ site

Tetrahedral SO$_4$$^{2-}$ site

1a octahedral M(H$_2$O)$_6$$^{2+}$ site

Fig. 11. Unit-strain tensor representation glyphs indicating the structural response to changing either the 1a- or 1b-site cation from Mg to Co or Mn. Green portions of the tensor representation surface indicate positive strains whereas red areas indicate negative strains. Figures plotted using *WinTensor* [40] and post-processed with *MeshConv* (courtesy Patrick Min), and *MeshLab* (http://meshlab.sourceforge.net).

Table 4

Dimensions and distortion metrics (after [62] for the SO_4^{2-} and $M(H_2O)_6$ polyhedra in each of the various DFT structural models. Reproducibility in the calculations may be judged from the standard deviation of the sulfate tetrahedron's metrics: bond lengths $\pm\, 3 \times 10^{-4}$ Å; volumes $\pm\, 1 \times 10^{-3}$ Å^3; bond angle variance $\pm\, 4 \times 10^{-2}$ deg^2.

	Pure Mg meridianiite	Co on 1a	Co on 1b	Mn on 1a	Mn on 1b
Sulfate tetrahedron					
Mean S–O	1.4903	1.4899	1.4900	1.4904	1.4907
Volume	1.6986	1.6970	1.6975	1.6989	1.6998
Dist. Index	0.0057	0.0057	0.0059	0.0058	0.0058
Quad. Elong.	1.0001	1.0001	1.0001	1.0001	1.0001
Bond Angle Var.	0.32	0.28	0.38	0.34	0.30
1a octahedral site		Co on 1a		Mn on 1a	
Mean M–O	2.0929	2.1896	2.0943	2.2120	2.0950
Volume	12.120	13.898	12.213	14.395	12.232
Dist. Index	0.0065	0.0142	0.0086	0.0082	0.0062
Quad. Elong.	1.0015	1.0049	1.0020	1.0018	1.0016
Bond Angle Var.	4.99	15.61	6.47	5.69	5.30
1b octahedral site			Co on 1b		Mn on 1b
Mean M–O	2.1019	2.0988	2.1905	2.1018	2.2194
Volume	12.364	12.311	13.921	12.365	14.560
Dist. Index	0.0195	0.0199	0.00172	0.0185	0.0232
Quad. Elong.	1.0012	1.0013	1.0048	1.0012	1.0014
Bond Angle Var.	1.13	1.41	15.28	1.66	0.70

Table 5

Hydrogen bond lengths and change relative to the pure Mg-analogue (%) for each of the various DFT structural models.

	Pure Mg meridianiite	Co on 1a	Δ (%)	Co on 1b	Δ (%)	Mn on 1a	Δ (%)	Mn on 1b	Δ (%)
H-bonds donated by water molecules coordinated to the cation on the 1a site									
H1a···O1	1.8388	1.8114	(-1.5)	1.8276	(-0.6)	1.8151	(-1.3)	1.8459	(0.4)
H1b···Ow8	1.6725	1.7025	(1.8)	1.6716	(-0.1)	1.6786	(0.4)	1.6773	(0.3)
H2a···O1	1.8103	1.7885	(-1.2)	1.8037	(-0.4)	1.8094	(0.0)	1.8135	(0.2)
H2b···Ow8	1.6737	1.6518	(-1.3)	1.6754	(0.1)	1.6657	(-0.5)	1.6817	(0.5)
H3a···Ow11	1.7945	1.7888	(-0.3)	1.7985	(0.2)	1.7927	(-0.1)	1.7887	(-0.3)
H3b···O1	1.8580	1.7976	(-3.3)	1.8634	(0.3)	1.8212	(-2.0)	1.8601	(0.1)
Average			(-1.0)		(-0.1)		(-0.6)		(0.2)
H-bonds donated / accepted by water molecules coordinated to the cation on the 1b site									
H4a···Ow9	1.6130	1.6134	(0.0)	1.5688	(-2.7)	1.6172	(0.3)	1.6010	(-0.7)
H4b···Ow11	1.7562	1.7594	(0.2)	1.7499	(-0.4)	1.7487	(-0.4)	1.7399	(-0.9)
H5a···Ow7	1.6985	1.6957	(-0.2)	1.7156	(1.0)	1.7023	(0.2)	1.6896	(-0.5)
H5b···Ow9	1.7216	1.7083	(-0.8)	1.7199	(-0.1)	1.7243	(0.2)	1.7265	(0.3)
H6a···Ow10	1.6851	1.6871	(0.1)	1.6705	(-0.9)	1.6839	(-0.1)	1.6890	(0.2)
H6b···Ow7	1.6809	1.6729	(-0.5)	1.6558	(-1.5)	1.6824	(0.1)	1.6643	(-1.0)
H7b···Ow4	1.7243	1.7229	(-0.1)	1.7076	(-1.0)	1.7258	(0.1)	1.6873	(-2.1)
Average			(-0.2)		(-0.8)		(0.0)		(-0.7)
H-bonds donated by 'interstitial' water molecules									
H7a···O2	1.7646	1.7574	(-0.4)	1.7935	(1.6)	1.7649	(0.0)	1.7761	(0.7)
H7b···Ow4	1.7243	1.7229	(-0.1)	1.7076	(-1.0)	1.7258	(0.1)	1.6873	(-2.1)
H8a···O3	1.8207	1.8067	(-0.8)	1.8093	(-0.6)	1.8224	(0.1)	1.8301	(0.5)
H8b···O4	1.6938	1.7030	(0.5)	1.6865	(-0.4)	1.6940	(0.0)	1.6958	(0.1)
H9a···O3	1.7395	1.7353	(-0.2)	1.7151	(-1.4)	1.7389	(0.0)	1.7363	(-0.2)
H9b···Ow10	1.6238	1.6217	(-0.1)	1.6173	(-0.4)	1.6313	(0.5)	1.6288	(0.3)
H10a···O4	1.6278	1.6307	(0.2)	1.6399	(0.7)	1.6352	(0.5)	1.6332	(0.3)
H10b···O2	1.7201	1.7281	(0.5)	1.7076	(-0.7)	1.7281	(0.5)	1.7245	(0.3)
H11a···O2	1.8492	1.8289	(-1.1)	1.8292	(-1.1)	1.8427	(-0.4)	1.8604	(0.6)
H11b···O3	1.7866	1.7879	(0.1)	1.7830	(-0.2)	1.7957	(0.5)	1.7850	(-0.1)
Average			(-0.1)		(-0.3)		(0.2)		(0.0)

Mn substitution produces either small positive or negative strains subparallel to $b*$ and a more uniform positive strain orthogonally. It is satisfying to discover that the unit-strain representation surfaces in Fig. 11 share some important characteristics with the same quantities derived experimentally from flash-frozen aqueous solutions of Co- and Mn-doped $MgSO_4$ (bottom of Fig. 11, redrawn from data in Ref. [20]). Experimentally, cobalt substitution leads to a large lobe of negative strain subparallel with $b*$ and a much smaller lobe of positive strain subparallel with the c-axis. The observed volume strain is negative (i.e., cobalt substitution reduces the unit-cell volume in the real material) whereas the DFT-calculated volume strain is positive, but the overall spatial distribution is in good agreement with a model in which most of the Co is on the $1b$ site.

Starting with the local coordination of each cation, we see from Table 4 that Co substitution increases the octahedral site volume by ~14% and Mn substitution by ~17%, but this is where the similarities end. Whilst effecting the greatest octahedral 'inflation', Mn substitution does little to alter the distance/angular distortion metrics. Conversely, Co substitution alters these metrics substantially with respect to the Mg-meridianiite structure. This octahedral distortion is attributable to a weak Jahn-Teller effect from the high-spin $3d^7$ Co^{2+} ion, which is absent for the high-spin $3d^5$ Mn^{2+} ion.

The change in hydrogen bond length (used as a proxy for H-bond strength) is also indicative (Table 5). Hydrogen bonds donated, or in one instance accepted, by cation-coordinated water become shorter (stronger) when Mg is replaced by either Co ($\Delta L = -0.8$ to -1.0%) or Mn ($\Delta L = -0.6$ to -0.7%). Of the hydrogen bonds donated by interstitial water molecules, Ow7 through Ow11, only the one that is donated to a cation-coordinated water, H7b···Ow4, changes in length significantly. This supports our earlier hypothesis that a relocation of charge from the cation out into the hydrogen bonds between the cation's first and second nearest neighbours.

4. Conclusions

The ternary systems $CoSO_4$–$MgSO_4$–H_2O and $MnSO_4$–$MgSO_4$–H_2O have been studied at 270 K and solubility phase diagrams representative of crystallisation under conditions of isothermal evaporation have been obtained. We report the partitioning of macro-amounts of dopant cations Co^{2+} and Mn^{2+} into the structure of meridianiite for the first time and reveal that each cation exhibits significantly different octahedral site preferences in the structure. Our results confirm the temperature dependence of the partitioning of Mg into the bieberite structure. No evidence of other hydration states (e.g., 9H_2O) was observed. DFT calculations largely support the observed difference in site occupancy preference between Co and Mn and provide insight into the mechanism.

Identifying these materials in nature is likely to be non-trivial, since they will be have limited spatial and temporal abundance, be prone to dehydration in air even at low temperatures, be friable when formed by efflorescence, and will require cryogenic storage, transport and X-ray diffraction analysis. Where highly hydrated salts containing $CoSO_4$ or $MnSO_4$ occur, they tend to develop as fibrous efflorescences in cool high-humidity environments, often being protected from short-to long-term variations in temperature by virtue of being underground, either in caves or mines. The lack of any reported occurrence of Co- or Mn-bearing meridianiite may then be due simply to the difficulty in identification.

Acknowledgements

Appendix A. Supplementary data

Supplementary data related to this article can be found at http://dx.doi.org/10.1016/j.fluid.2017.01.005.

References

[1] T. Akamatsu, K. Fujino, M. Kumazawa, A. Fujimura, M. Kato, H. Sawamoto, T. Yamanaka, Pressure effect on the divalent cation distribution in nonideal solid solution of forsterite and fayalite, Phys. Chem. Min 16 (1988) 105–113.

[2] C. Balarew, V. Karaivanova, S. Aslanian, Isomorphic relations among the heptahydrate sulfates of single divalent metals (Mg^{2+}, Zn^{2+}, Ni^{2+}, Fe^{2+}, Co^{2+}), Krist. Tech 8 (1973) 115–125.

[4] A. Benrath, A. Blankenstein, Über mischkristalle in der vitriolreihe, I. Z. Anorg. Allgem. Chem 216 (1933) 41–48.

[5] K.M. Cannon, Spotted Lake: Analog for Hydrated Sulfate Occurrences in the Last Vestiges of Evaporating Martian Paleolakes, PhD Thesis, Queen's University, Ontario, 2012.

[6] G.H. Cheeseman, E.K. Nunn, Algebraic extrapolation in ternary systems, Aust. J. Chem 17 (1964) 399–405.

[7] J. Chen, W. X, A. Sellon, Electronic structure and bonding properties of cobalt oxide in the spinel structure, Phys. Rev. B 83 (2011) 245204.

[8] H. Chihara, S. Seki, Studies of crystalline hydrates. II. Thermal transition and dehydration of Ni-, Fe-, Co-, Zn-, Mn-, and Mg-sulfate hydrates, Bull. Chem. Soc. Jpn 26 (1953) 88–92.

[9] S.J. Clark, M.D. Segall, C.J. Pickard, P.J. Hasnip, M.I.J. Probert, K. Refson, M.C. Payne, First principles methods using CASTEP, Z. Krist 220 (2005) 567–570.

[10] F.G. Cottrell, On the solubility of manganous sulphate, J. Phys. Chem 4 (1900) 637–656.

[11] W.–D. Deckwer, Density, viscosity, vapor pressure, and hydrogen solubility of aqueous manganese(II) sulfate solutions, J. Chem. Eng. Data 25 (1980) 75–76.

[12] S.L. Dudarev, G.A. Botton, S.Y. Savrasov, C.J. Humphreys, A.P. Sutton, Electron-energy-loss spectra and the structural stability of nickel oxide: an LSDA+U study, Phys. Rev. B 57 (1998) 1505–1509.

[13] H.H. Emons, G. Ziegenbalg, R. Naumann, F. Paulik, Thermal decomposition of the magnesium sulphate hydrates under quasi-isothermal and quasi-isobaric conditions, J. Therm. Anal 36 (1990) 1265–1279.

[14] W.C. Feldman, M.T. Mellon, S. Maurice, T.H. Prettyman, J.W. Carey, D.T. Vaniman, D.L. Bish, C.I. Fialips, S.J. Chipera, J.S. Kargel, R.C. Elphic, H.O. Funsten, D.J. Lawrence, R.L. Tokar, Geophys. Res. Lett 31 (2004a) article L16702.

[15] W.C. Feldman, T.H. Prettyman, S. Maurice, J.J. Plaut, D.L. Bish, D.T. Vaniman, M.T. Mellon, A.E. Metzger, S.W. Squyres, S. Karunatillake, W.V. Boynton, R.C. Elphic, H.O. Funsten, D.J. Lawrence, R.L. Tokar, J. Geophys. Res. Planets 109 (2004b) article E09006.

[16] A.D. Fortes, X-ray powder diffraction analysis of two new magnesium selenate hydrates, $MgSeO_4 \cdot 9H_2O$ and $MgSeO_4 \cdot 11H_2O$, Powder Diffr 30 (2015) 149–157.

[17] A.D. Fortes, I.G. Wood, X-ray powder diffraction analysis of a new magnesium chromate hydrate, $MgCrO_4 \cdot 11H_2O$, Powder Diffr. 27 (2012) 8–11.

[18] A.D. Fortes, D. Alfè, E.R. Hernández, M.J. Gutmann, Crystal structure of magnesium selenate enneahydrate, $MgSeO_4 \cdot 9H_2O$, from 5–250 K using neutron time-of-flight Laue diffraction, Acta Cryst. B 71 (2015) 313–327.

[19] A.D. Fortes, F. Browning, I.G. Wood, Cation substitution in synthetic meridianiite ($MgSO_4 \cdot 11H_2O$) I: X-ray powder diffraction analysis of quenched polycrystalline aggregates, Phys. Chem. Mineral. 39 (2012a) 419–441.

[20] A.D. Fortes, F. Browning, I.G. Wood, Cation substitution in synthetic meridianiite ($MgSO_4 \cdot 11H_2O$) II: variation in unit-cell parameters determined from X-ray powder diffraction data, Phys. Chem. Mineral. 39 (2012b) 443–454.

[21] A.D. Fortes, I.G. Wood, M.J. Gutmann, $MgSO_4 \cdot 11H_2O$ and $MgCrO_4 \cdot 11H_2O$ from time-of-flight neutron single-crystal Laue data, Acta Cryst. C 69 (2013) 324–329.

[22] A.D. Fortes, I.G. Wood, K.S. Knight, The crystal structure and thermal expansion tensor of $MgSO_4 \cdot 11D_2O$ (meridianiite) determined by neutron powder diffraction, Phys. Chem. Min. 35 (2008) 207–221.

[23] A.D. Fortes, I.G. Wood, L. Vočadlo, H.E.A. Brand, K.S. Knight, Studies of anhydrous magnesium sulfate polymorphs. I: structures and thermal expansion of α-$MgSO_4$ and β-$MgSO_4$ from 4.2–300 K by powder neutron diffraction, J. Appl. Cryst. 40 (2007) 761–770.

[24] A.D. Fortes, K.S. Knight, I.G. Wood, Structure, thermal expansion and incompressibility of $MgSO_4 \cdot 9H_2O$, its relationship to meridianiite ($MgSO_4 \cdot 11H_2O$) and possible natural occurrences, Acta Cryst. B 73 (2017a), http://dx.doi.org/10.1107/S2052520616018266.

[25] A.D. Fortes, F. Fernandez-Alonso, M.G. Tucker, I.G. Wood, Isothermal equation of state and high-pressure phase transitions of synthetic meridianiite ($MgSO_4 \cdot 11D_2O$) determined by neutron powder diffraction and quasielastic neutron spectroscopy, Acta Cryst. B 73 (2017b), http://dx.doi.org/10.1107/S2052520616018254.

[26] R.S. Gärtner, F.E. Genceli, D.O. Trambitas, G.J. Witkamp, Impurity gradients in solution-grown ice and crystals measured by cryo-laser ablation and high-resolution-induced-coupled plasma mass spectrograph, J. Cryst. Growth 275 (2005) e1773–e1778.

[27] F.E. Genceli, M. Lutz, A.L. Spek, G.-J. Witkamp, Crystallization and character-ization of a new magnesium sulfate hydrate $MgSO_4 \cdot 11H_2O$, Cryst. Growth Des. 7 (2007) 2460–2466.

[28] F.E. Genceli, H. Shinochirou, I. Yoshinori, S. Toshimitsu, T. Hondoh, T. Kawamura, G.-J. Witkamp, Meridianiite detected in ice, J. Glaciol. 55 (2009) 117–122.

[29] M.J. Gutmann, SXD2001. ISIS Facility, Rutherford Appleton Laboratory, Oxfordshire, England, 2005.

[30] J.M. Hammarstrom, R.R. Seal, A.L. Meier, J.M. Kornfeld, Secondary sulfate minerals associated with acid drainage in the eastern US: recycling of metals and acidity in surficial environments, Chem. Geol. 215 (2005) 407–431.

[31] Y.M.A. Hashash, J.I.–C. Yao, D.C. Wotring, Glyph and hyperstreamline repre-sentation of stress and strain tensors and material constitutive response, Int. J. Numer. Anal. Meth. Geomech. 27 (2003) 604–626.

[32] R.M. Hazen, R.T. Downs, C.T. Prewitt, Principles of comparative crystal chemistry, Rev. Min. Geochem 41 (2000) 1–33.

[33] M.H. Hey, On pink epsomites and fauserite, Min. Mag. 22 (1931) 510–518.

[34] C. Himawan, G.-J. Witkamp, Crystallization kinetics of $MgSO_4 \cdot 12H_2O$ from different scales of batch cooling scraped crystallizers, Cryst. Res. Technol. 9 (2006) 865–873.

[35] C. Himawan, H.J.M. Kramer, G.J. Witkamp, Study on the recovery of purified $MgSO_4 \cdot 7H_2O$ crystals from industrial solutions by eutectic freezing, Sep. Pur. Tech. 50 (2006) 240–248.

[36] R. Hodenberg, R. Kühn, Zur Kenntnis der Magnesiumsulfathydrate und der Effloreszenzen des Kieserits von Hartsalzen, Kali Steinsalz 4 (1967) 326–340.

[37] P. Hohenberg, W. Kohn, Inhomogeneous electron gas, Phys. Rev. 136 (1964) B864–B871.

[38] J. Hubbard, Electron correlations in narrow energy bands, Proc. R. Soc. Lond. Ser. A – Math. Phys. Sci. 276 (1963) 238–257.

[39] J.L. Jambor, D.K. Nordstrom, C.N. Alpers, Metal-sulfate salts from sulfide mineral oxidation, Rev. Mineral. 40 (2000) 303–350.

[40] W. Kaminski, WinTensor 1.1, 2004. http://cad4.cpac.washington.edu/WinTensorhome/WinTensor.htm.

[41] J.S. Kargel, Brine volcanism and the interior structures of asteroids and icy satellites, Icarus 94 (1991) 369–390.

[42] D.A. Keen, M.J. Gutmann, C.C. Wilson, SXD - the single-crystal diffractometer at the ISIS spallation neutron source, J. Appl. Cryst. 39 (2006) 714–722.

[43] W. Kohn, L.J. Sham, Self-consistent equations including exchange and corre-lation effects, Phys. Rev. 140 (1965) A1133–A1138.

[44] H. Kroll, A. Kirfel, P. Sutanto, W. Kockelmann, M. Knapp, P. Schmid-Beurmann, A. Sell, J. Büscher, CoMg olivine: cation partitioning, thermal expansion and structural variation studied by in situ neutron and synchrotron powder diffraction, Eur. J. Min. 28 (2016), http://dx.doi.org/10.1127/ejm/2016/0028-2554.

[46] N.L. Lanza, 20 co-authors, High manganese concentrations in rocks at Gale crater, Mars, Geophys. Res. Lett. 41 (2014) 5755–5763.

[47] N.L. Lanza, 43 co-authors, Oxidation of manganese in an ancient aquifer, Kimberley formation, Gale crater, Mars. Geophys. Res. Lett. 43 (2016) 7398–7407, http://dx.doi.org/10.1002/2016GL069109.

[48] A.C. Larson, R.B. Von Dreele, General Structure Analysis System (GSAS), Los Alamos National Laboratory Report, LAUR, 2000, 86–748.

[49] M. Maneva, D. Rizova, L. Genov, G. Liptay, On the thermal decomposition of $NiSO_4 \cdot nH_2O$ ($n = 7,6,4,1$) and of their deuterated analogs, J. Therm. Anal. Calorim. 36 (1990) 915–922.

[50] G.M. Marion, M.V. Mironenko, M.W. Roberts, FREZCHEM: a geochemical model for cold aqueous solutions, Comp. Geosci. 36 (2010) 10–15.

[51] J. Majzlan, Advances and gaps in the knowledge of thermodynamics and crystallography of acid mine drainage sulfate minerals, Chimia 64 (2010) 699–704.

[52] T. Oikova, D. Barkov, The $CoSO_4$- $MgSO_4$-H_2O system at 40 °C, Russ. J. Inorg. Chem. 24 (1979) 278–280.

[53] T. Oikova, C. Balarew, L. Makarow, Thermodynamical study on the systems $MgSO_4$-$CoSO_4$-H_2O and $MgSO_4$-$ZnSO_4$-H_2O at 25,0°C, Russ. J. Inorg. Chem. 50 (1976) 347–352.

[54] M.C. Payne, M.P. Teter, D.C. Allan, T.A. Arias, J.D. Joannopoulos, Iterative minimization techniques for ab initio total energy calculations – molecular-dynamics and conjugate gradients, Rev. Mod. Phys. 64 (1992) 1045–1097.

[55] R.C. Peterson, R. Wang, Crystal molds on Mars: melting of a possible new mineral species to create martian chaotic terrain, Geology 34 (2006) 957–960.

[56] R.C. Peterson, W. Nelson, B. Madu, H.F. Shurvell, Meridianiite: a new species observed on Earth and predicted to exist on Mars, Am. Mineral. 92 (2007) 1756–1759.

[57] B.G. Pfrommer, M. Cote, S.G. Louie, M.L. Cohen, Relaxation of crystals with the quasi-Newton method, J. Comp. Phys. 191 (1997) 233–240.

[58] V. Pillay, R.S. Gärtner, C. Himawan, M.M. Seckler, A.E. Lewis, G.-J. Witkamp, $MgSO_4 + H_2O$ system at eutectic conditions and thermodynamic solubility products of $MgSO_4 \cdot 12H_2O(s)$ and $MgSO_4 \cdot 7H_2O(s)$, J. Chem. Eng. Data 50 (2005) 551–555.

[59] H. Putz, K. Brandenburg, Diamond - crystal and molecular structure visuali-zation. Crystal impact - GbR, Kreuzherrenstr 102 (2006) 53227. Bonn, Ger-many, http://www.crystalimpact.com/diamond.

[60] D.G. Randall, J. Nathoo, A succinct review of the treatment of reverse osmosis brines using freeze crystallization, J. Water Process Eng. 8 (2015) 186–194.

[61] S.A.T. Redfern, K.S. Knight, C.M.B. Henderson, B.J. Wood, Fe-Mn cation ordering in fayalite-tephroite ($Fe_xMn_{1-x})_2SiO_4$ olivines: a neutron diffraction study, Min. Mag. 62 (1998) 607–615.

[62] K. Robinson, G.V. Gibbs, P.H. Ribbe, Quadratic elongation: a quantitative measure of distortion in coordination polyhedra, Science 172 (1971) 567–570.

[63] T. Sakurai, Y. Iizuka, S. Horikawa, S. Johnsen, D. Dahl-Jensen, J.P. Steffensen, T. Hondoh, Direct observation of salts as micro-inclusions in the Greenland GRIP ice core, J. Glaciol. 55 (2009) 777–783.

[64] H. Schott, A mathematical extrapolation for the method of wet residues, J. Chem. Eng. Data. 6 (1961) 324.

[65] F.A.H. Schreinemakers, Graphische ableitungen aus den lösungs-isothermen eines doppelsalzes und seiner komponenten, Z. Phys. Chem. 11 (1893) 75–109.

[66] V.F. Sears, Neutron scattering lengths and cross sections, Neutron news 3 (1992) 29–37.

[67] M.D. Segall, P.J.D. Lindan, M.J. Probert, C.J. Pickard, P.J. Hasnip, S.J. Clark, M.C. Payne, First-principles simulation: ideas, illustrations and the CASTEP code, J. Phys. Cond. Matter 14 (2002) 2717–2744.

[68] R.D. Shannon, Revised effective ionic radii and systematic studies of inter-atomic distances in halides and chalcogenides, Acta Cryst. A 32 (1976) 751–767.

[69] S.G. Sinha, N.D. Deshpande, D.A. Deshpande, Dehydration of crystalline $CoSO_4 \cdot 7H_2O$, Thermochim. Acta 156 (1989) 1–10.

[70] S.G. Sinha, N.D. Deshpande, D.A. Deshpande, Dehydration of crystalline $MnSO_4 \cdot 4H_2O$, Thermochim. Acta 113 (1987) 95–104.

[71] E. Tobler, Ueber die Löslichkeit einiger schwefelsauren Salze der Magnesiar-eihe in Wasser, Ann. Chem. Pharm. 95 (1855) 193–199.

[72] B.H. Toby, EXPGUI, a graphical user interface for GSAS, J. Appl. Cryst. 34 (2001) 210–213.

[73] I.G. Wood, N. Hughes, F. Browning, A.D. Fortes, A compact, transportable, thermoelectrically-cooled cold stage for reflection geometry X-ray powder diffraction, J. Appl. Cryst. 45 (2012) 608–610.

[74] Z. Wu, R.E. Cohen, More accurate generalized gradient approximation for solids, Phys. Rev. B 73 (2006) article 235116.

[75] B.I. Zhelnin, G.I. Gorshtein, Equilibrium in $MnSO_4$-$Mgso_4$-H_2O system at 25° and 100 °C, Russ. J. Inorg. Chem. 16 (1971) 1668–1670.

[76] F. Zhou, M. Coccioni, C.A. Marianetti, D. Morgan, G. Ceder, First Principles predictions of redox potentials in transition metals with LDA+U, Phys. Rev. B 70 (2004) 235121.